Dynamics in the ordered and disordered phases of barocaloric adamantane

Bernet E. Meijer,[a], Richard J. Dixey,[a] Franz Demmel,[b] Robin Perry,[c]
Helen C. Walker,[b†] and Anthony E. Phillips[a*]

Electronic Supplementary Information

Contents

*a.e.phillips@qmul.ac.uk
†helen.c.walker@stfc.ac.uk

S1 Extrapolation of calorimetric data

The barocaloric behaviour at low pressures is estimated by extrapolating the high-pressure heat flow peak of 1000 bar to lower pressures. As is shown in table S1, the isothermal entropy change, given by $dS = \int dQ/TdT$, is roughly constant with pressure. Therefore, the extrapolated heat flow peaks were scaled to account for the decrease in phase transition enthalpy at low temperatures and ensure that the isothermal entropy change remains the same. Thanks to the scaling, it does not matter which heat flow peak is chosen for extrapolation, so the 1000 bar peak was chosen arbitrarily. The extrapolated heat flow peaks and scaled entropy changes are shown in figure S1.

P (bar)	ΔS_{iso} ($\mathrm{JK^{-1}kg^{-1}}$)
900	120.44
925	119.58
950	119.50
975	119.94
1000	121.59

Table S1: Maximum isothermal entropy changes at high pressure. The entropy changes do not show any obvious pressure dependence.

Figure S1 shows that the width of the *measured* heat flow peaks increases with pressure. While this won't affect the maximum isothermal entropy change, it might affect the temperature range of *unsaturated* isothermal entropy changes, as it changes the steepness of the slopes in figures S1c and d. However the main result of this work, i.e. fully saturated reversible effects at 200 bar, will remain unchanged.

It is worthwhile to note that the shape of the heat flow peaks might depend on many different factors. For the present measurements, the increased broadening of the peaks with pressure might be accounted for by realising that different parts of the material (such as the bulk and edges) can respond slightly differently to temperature, causing a broadening of the heat flow peaks. At higher pressures, this effect might be amplified, leading to increased broadening with pressure. In general however, the shape of the heat flow peaks will also depend on the heating rate, so it is hard to make general claims about the shape of the peaks. Finally, since these measurements are quasi-direct, it is difficult to say what a heat flow peak will look like in a real application, where heat flow is produced by pressurisation rather than changing temperature.

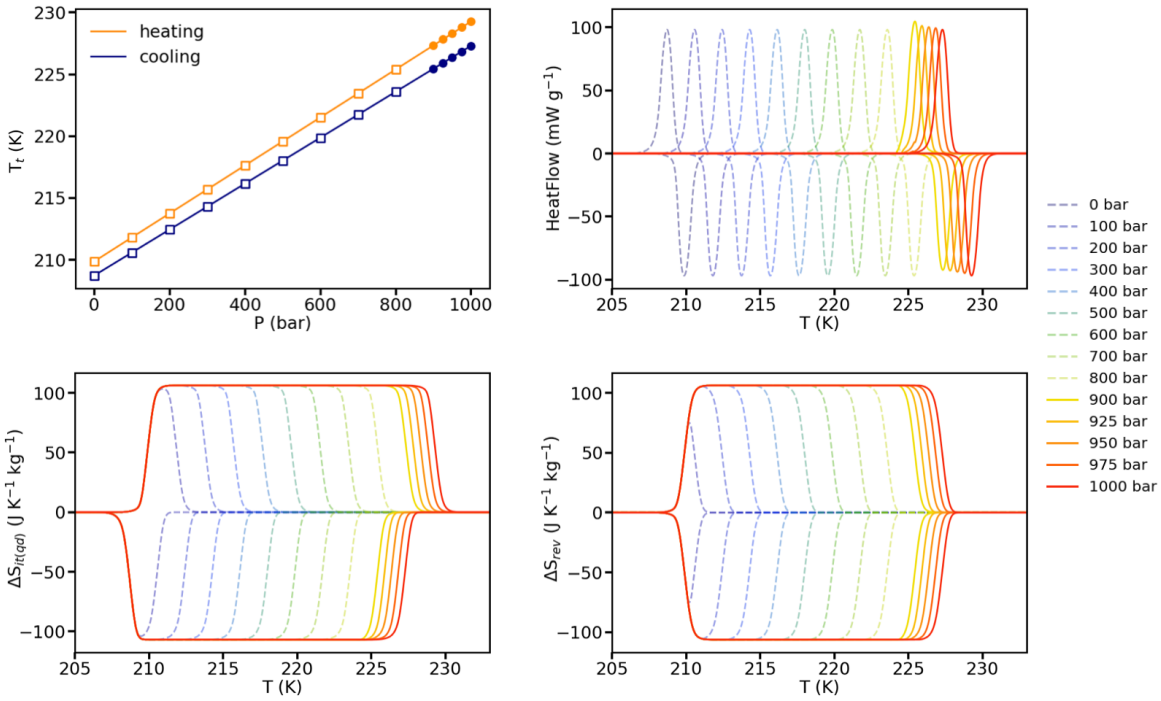

Figure S1: Details of the extrapolation of calorimetric data. (a) The phase diagram as deduced from heat-flow measurements: solid circles are experimental data points, open squares are extrapolated datapoints (based on a linear fit to the experimental data) at which the low-temperature barocaloric behaviour will be estimated. (b) Heat flow data at low pressures have been simulated by shifting the heat flow peaks from the high-pressure measurements to the predicted phase transition temperatures in (a). Solid lines are experimental data and the dotted lines are simulated. (c) The heat flow peaks are integrated and each heat flow integral for $p > 0$ is then subtracted off the heat flow integral for $p = 0$. The resulting isothermal entropy change entropy change $\Delta S_{\mathrm{it(qd)}}$ for $0 \rightarrow p$ and $p \rightarrow 0$ was scaled to correct for the increase in phase transition enthalpy at high temperatures. (d) Reversible entropy change ΔS_{rev} for $0 \rightarrow p$ and $p \rightarrow 0$ deduced from (c). The simulated data predict that it is possible to get reversible barocaloric effects for pressures < 100 bar, with saturation already at < 200 bar.

S2 Inelastic neutron scattering

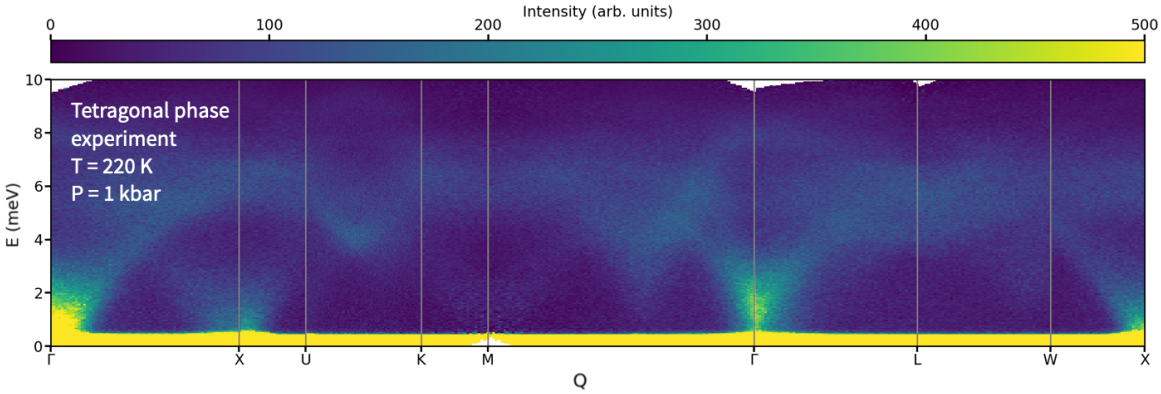

Figure S2: Dispersion curve in adamantane's ordered tetragonal phase, measured by single-crystal inelastic neutron scattering at $T = 220$ K and $P = 1$ kbar.

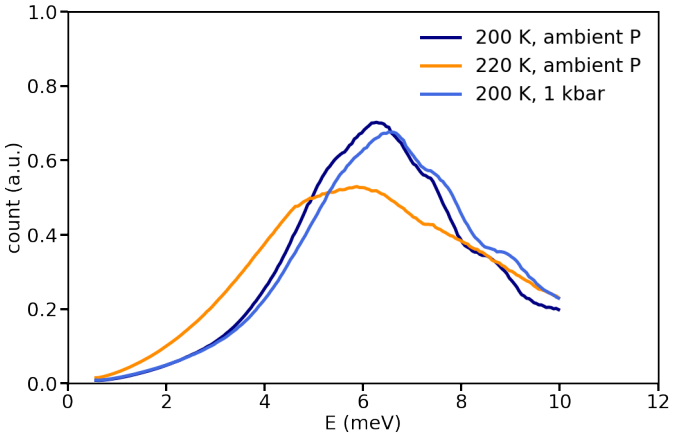

Figure S3: Experimental 1-phonon density of states. There is clear softening in the high-temperature cubic phase (220 K, ambient P) and in the tetragonal phase, the modes are stiffer at the (T=220 K, P=1 kbar) phase point than at the (T=200 K, P=ambient) phase point, likely because high pressure restricts the molecules' movements.

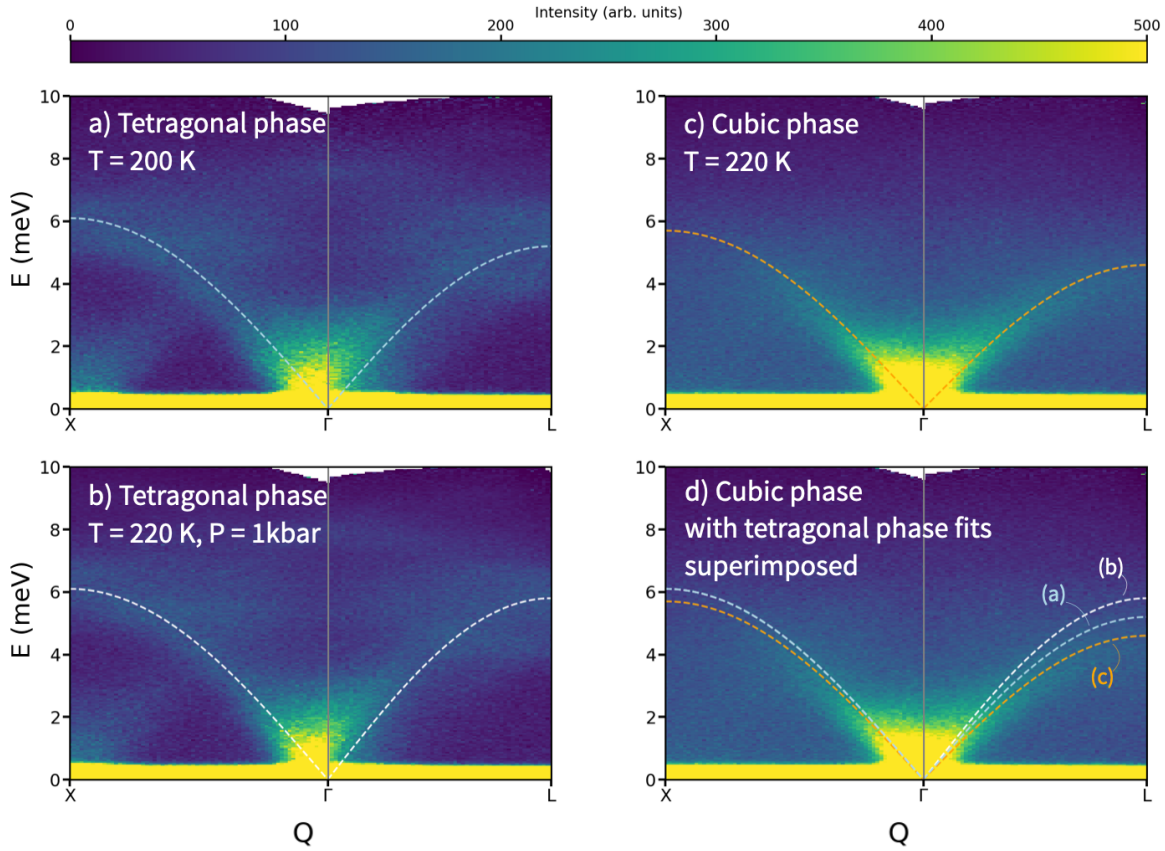

Figure S4: Acoustic modes in the experimental dispersion curves in (a) the tetragonal phase at low temperature, (b) the tetragonal phase at high pressure and (c) the cubic phase. The acoustic modes have been fitted to the eye with a sine wave of variable amplitude. The image in (d) is the cubic phase, with the fits of all phases superimposed. It shows (1) that the acoustic modes have softened in the cubic phase and (2) that the modes are stiffer in the tetragonal phase at high pressure (b) than at low temperature (a). The latter is consistent with the density of states (figure S3).

S3 Quasielastic neutron scattering under high pressure

S3.1 Results

The model describing the quasielastic signal in adamantane's high-temperature phase has been uncovered by Bee *et al.*[1] and attributed to C_4 rotational jumps. In the analysis of the pressure data collected in this work, this rotational model is therefore used to fit the data. The free model parameters are τ_{C_4} (the average time between jumps), f (empirical fitting parameter to account for the fraction of rotating molecules), an arbitrary scaling factor $C(Q)$ (which accounts, among others, for the Debye-Waller factor) and a background term $B(Q,\omega)$ that is assumed to be linear in the energy ω. The full model is given below.

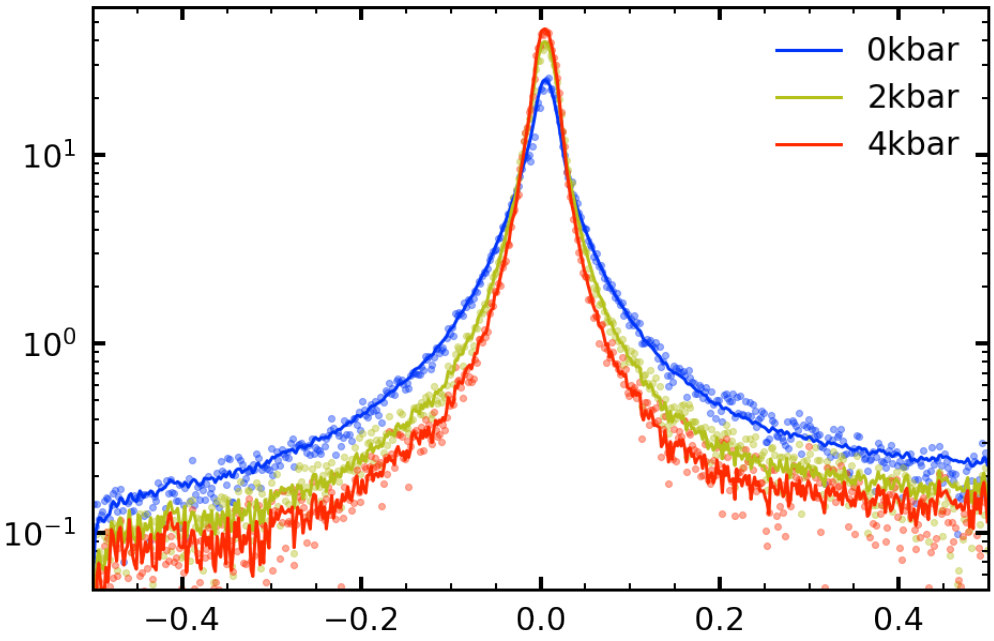

Figure S5: Quasi-elastic broadening in adamantane's disordered cubic phase is suppressed under pressure. Data is collected at $T = 300$ K. The spectra have been summed over all Å^{-1}< Q <2 Å^{-1}. The experimental data are represented by dots and the corresponding fit by lines. (The fits itself contain noise due to convolution with the experimental resolution.)

The resulting fit to the pressure data is shown in figure S5. Here the spectra have been summed over all momentum transfer Q, to increase the signal-to-noise ratio and aid visualisation. The quasielastic broadening is suppressed by pressure. This is the result of two changing model parameters in the fit: both the frequency of C_4 jumps and the fraction of rotating molecules decrease with pressure, as

shown in table S5.

T (K)	P (kbar)	τ_{C_4} (ps)	f
220	0	50.9	0.5
300	0	18.8	0.7
300	2	33.8	0.6
300	4	50.2	0.4

Table S2: Mean residence times τ_{C_4} and fraction of dynamically activated molecules as determined from a least-squares fit to the experimental spectra.

S3.2 C_4 rotational jump model

The scattering function for the cubic rotational dynamics of adamantane molecules is given by an elastic contribution (represented by the delta function) plus a sum of inelastic contributions (represented by Lorentzians)[2]:

$$S(Q,\omega) = A_0(Q,f)\delta(\omega) + \sum_i A_i(Q,f)\frac{1}{\pi}\frac{1/\tau_i(\tau_{C_4})}{(1/\tau_i(\tau_{C_4}))^2+\omega^2} \tag{1}$$

The amplitudes $A_i(Q,f)$ are given by [1,2]

$$A_0(Q,f) = 1 - f + \frac{f}{24}(1+2A+B+C+2D) \tag{2}$$

$$A_1(Q,f) = \frac{f}{24}(1+2A+B-C-2D) \tag{3}$$

$$A_2(Q,f) = \frac{f}{24}(4-4A+4B) \tag{4}$$

$$A_3(Q,f) = \frac{f}{24}(9-3B+3C-6D) \tag{5}$$

$$A_4(Q,f) = \frac{f}{24}(9-3B-3C+6D) \tag{6}$$

Where f is the fraction of rotating molecules, and

$$A = \sum_{\nu=1}^{4} J_\nu \tag{7}$$

$$B = \sum_{\nu=5}^{7} J_\nu \tag{8}$$

$$C = \sum_{\nu=8}^{13} J_\nu \tag{9}$$

$$D = \sum_{\nu=14}^{16} J_\nu. \tag{10}$$

$J_\nu = j_0(Qr_\nu$, with $j_0(x)$ the spherical Bessel function of zeroth order and r_ν the distances between initial and final positions of atoms after various cubic rotations, calculated by Lechner and Heidemann [3]. The Lorentzian widths $\tau_i(\tau_{C_4})$ are given by

$$\frac{1}{\tau_1} = 0, \tag{11}$$

$$\frac{1}{\tau_2} = \frac{2}{\tau_{C_4}}, \tag{12}$$

$$\frac{1}{\tau_3} = \frac{1}{\tau_{C_4}}, \tag{13}$$

$$\frac{1}{\tau_4} = \frac{2}{3\tau_{C_4}}, \tag{14}$$

$$\frac{1}{\tau_5} = \frac{4}{3\tau_{C_4}}. \tag{15}$$

The theoretical scattering function has been fitted to the reduced experimental quasielastic spectra $S_{\mathrm{exp}}(Q,\omega)$ using

$$S_{\mathrm{exp}}(Q,\omega) = R(\omega) \otimes (C(Q)S(Q,\omega)) + B(Q,\omega), \tag{16}$$

The factor $C(Q)$ includes the Debye-Waller factor $e^{-\langle u^2\rangle Q^2}$, where the mean-square displacement $\langle u^2\rangle$ represents molecular vibrations and librations. $C(Q)$ was allowed to vary freely with Q in the global fit. The model is convolved with the experimental resolution function $R(\omega)$ (collected with a low-temperature measurement) and a background term $B(Q,\omega)$ is added to account for inelastic contributions to the measured signal, which in this small energy range can be approximated as a linear function in energy.

S4 Lattice dynamics calculations

S4.1 Details of the methodology

S4.1.1 Energy minimisation

Before the dynamical matrix was diagonalised, the energy of the system was minimised. The forcefield parameters are given in table S3.

In the low-temperature phase, the energy of the unit cell was minimised using the default Newton-Raphson method in GULP with a Broyden-Fletcher-Goldfarb-Shanno (BFGS)[4] Hessian updating scheme.

In the high-temperature phase, an $8 \times 8 \times 8$ supercell (of FCC unit cells) was chosen, with a random distribution of the two possible orientations of the molecules. Finding a global energy minimum in this system proved difficult. We therefore used a combination of different algorithms to get as close to a global minimum as possible:

1. energy minimisation using the conjugate gradients implementation in the large-scale atomic/molecular massively parallel simulator (LAMMPS) code[5]. An external pressure of 1 bar was set to allow the simulation box to change size isotropically during the minimisation process. The procedure was stopped when the energy could not be minimised any further; however, the forces do not fulfil the stopping criteria, which means that a global minimum has not been found;

2. energy minimisation using the conjugate gradients implementation in GULP. The cell vectors are allowed to vary individually. Similarly to the LAMMPS result, the procedure was stopped when the energy could no longer be minimised, although a global minimum was not found.

3. energy minimisation using the Newton-Raphson method in GULP. A limited-memory BFGS Hessian updating scheme was used, since calculating the full inverse Hessian in this large system ($\sim 53,000$ atoms) was not possible. Again, this procedure finished when the energy could no longer be minimised, without finding a global minimum.

Optimisation of a sample of disordered FCC *unit* cells using a Newton-Raphson method with standard BFGS or conjugate gradients was also unsuccessful, as was evidenced by the existence of imaginary frequencies after the dynamical matrix diagonalisation. Nevertheless, by sequentially optimising the supercell with the methods described above, these imaginary frequencies were reduced to ~ 580 modes in the supercell, and after projection only represent 6.1% of all intermolecular modes in the Brillouin zone. In the calculation of the phonon density of states, the absolute value of these modes was used as an approximation of their true energy. As seen in the supplementary material, including the imaginary modes has a minimal effect on the phonon density of states.

Table S3: Adamantane intermolecular nearest-neighbour Buckingham potential parameters[6].

Type	A (kJ mol^{-1})	ρ (Å)	C (kJ mol^{-1} Å^{-6})
C-C	359824.0	0.278	2374.42
C-H	38492.8	0.278	522.67
H-H	11715.2	0.267	113.93

S4.1.2 Lattice dynamics

For the low-temperature phase, the dispersion curve of figure 4b in the main text is calculated using the quasicubic unit cell. The dynamical matrix was diagonalised using GULP, after which the neutron-weighted phonon dispersion was obtained using the python package Euphonic[7]. Neutron weighting can alter the visibility of modes in the simulated phonon dispersion due to the varying coherent scattering cross-sections for different elements and due to the polarisation factor $\mathbf{Q}\cdot\mathbf{e}$ in the one-phonon neutron scattering function, where $\mathbf{Q}$ is the wavevector and $\mathbf{e}$ is the mode eigenvector. In the face-centred cubic (FCC) to tetragonal phase transition, crystal twinning can occur. In figure 4b in the main text this has been accounted for by taking a weighted average of the three possible twins; the weights were adjusted empirically to get the greatest similarity between calculation and experiment.

In figure 5 in the main text, both the low- and high-temperature phases were calculated using a supercell calculation followed by the band-unfolding method[8], described in the main text. For the high-temperature phase, this was necessary to take into account the disorder-induced phonon broadening; the low-temperature phase was calculated using the same method for consistency. Care must be taken when using a supercell of conventional rather than primitive unit cells. For the high-temperature phase, we use a supercell of N conventional FCC unit cells. However, the sum over l in eq. 1 (main text) is over the *primitive* unit cells, and there are additional allowed wavevectors in the supercell[9], giving a total of $(4L)^3$ allowed wavevectors.

S4.1.3 Eigenvector analysis using GASP

Eigenvector analysis was performed with GASP[10,11], a software package that can, among other things, separate a molecular displacement into rotational and distortional components. For each eigenvector of the Γ-point calculation, the molecular structure was displaced along the eigenvector direction, with the average atomic displacement between 0.001 and 0.01 Å. (The calculation was repeated with a displacement $10\times$ larger, and yielded the same results. This means that the rotational/translational analysis is roughly independent of the displacement scale, at least for small displacements < 0.1Å.) The structure was consequently relaxed in GASP, which here means that distortional displacements were reversed (since we assume that adamantane is rigid and arbitrarily high force constants were

chosen, these distortional displacements are not meaningful). GASP's `netdr2` utility analyses, for each atom in each molecule, the total squared displacement:

$$M^2_{\text{tot, mole}} = \sum_i^{N_{\text{atoms}}} M_i^2 \tag{17}$$

where i sums over the atoms in the molecule and M_i^2 is the atomic displacement of atom i. Next, the `polycomp` utility analyses the squared displacement due to molecular rotation:

$$M^2_{\text{rot, mole}} = \sum_i^{N_{\text{atoms}}} M^2_{i,\text{rot}} \tag{18}$$

where $M^2_{i,\text{rot}}$ is the displacement of atom i due to molecular rotation. We define the rotational character as $M_{\text{rot}}/M_{\text{tot}}$.

S4.2 Unstable phonon modes

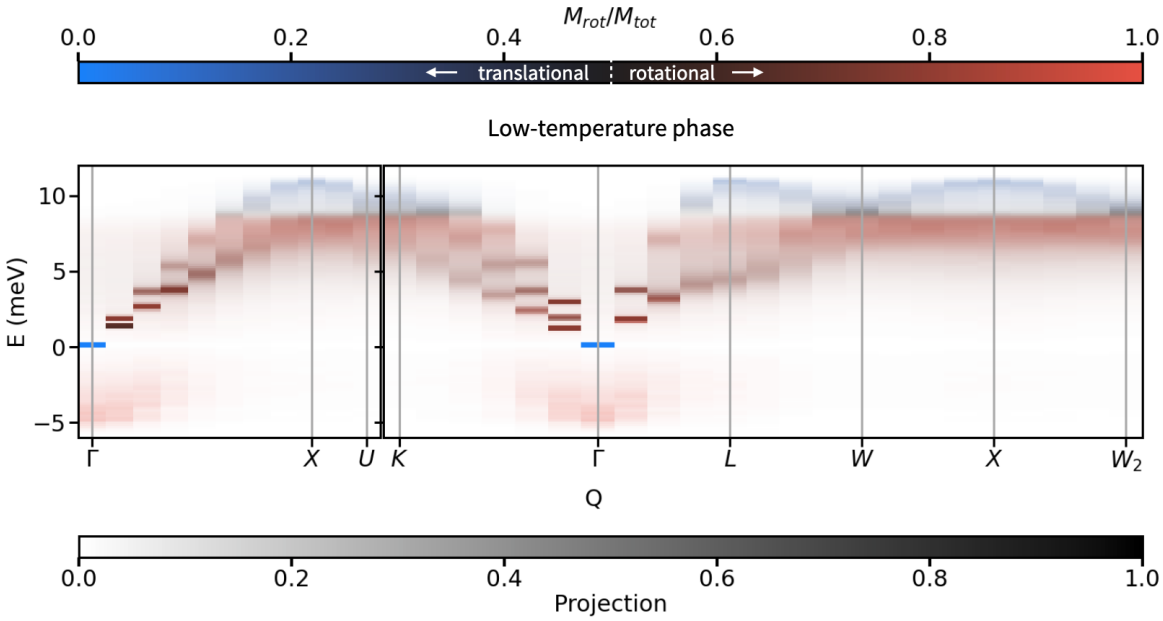

Figure S6: Dispersion curve in adamantane's disordered cubic phase calculated with supercell lattice dynamics. The imaginary frequencies have been plotted as negative frequencies. Each mode is coloured by its rotational character $M_{\mathrm{rot}}/M_{\mathrm{tot}}$. The imaginary frequencies correspond to purely rotational molecular movements.

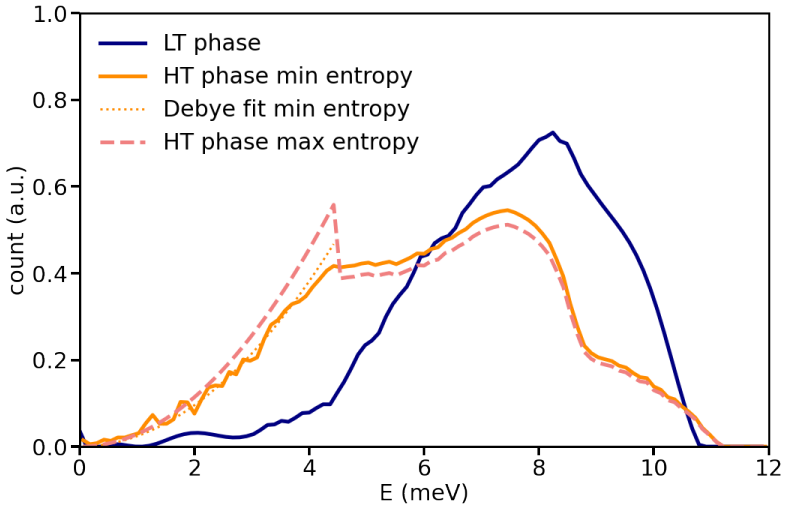

Figure S7: Calculated phonon density of states (pDOS) in adamantane's phases. In each phase, phonons were calculated at the Γ-point in a supercell ($8 \times 8 \times 8$ for high-temperature phase, $6 \times 6 \times 6$ for low-temperature phase) and projected onto the Brillouin zone; next, the projected intensities were integrated over the Brillouin zone to produce the pDOS. For the low-temperature phase, the density of states was also calculated with conventional methods (sampling the Brillouin zone with a uniform $16 \times 16 \times 16$ k-grid) and yielded similar results both in the shape of the pDOS and the calculated entropy (for SCLD method: $S_{\text{vib, LT}} = 695.78$ JK^{-1}kg^{-1}; for sampling method: $S_{\text{vib, LT}} = 691.24$ JK^{-1}kg^{-1}). The SCLD method is plotted here for consistency; this is also what is used to calculate the entropy change quoted in the main text. The high-temperature phase calculation resulted in imaginary frequencies. Here the DOS is plotted in two extremes: 1) the minimum entropy case, where the unstable modes are simply ignored, and 2) the maximum entropy case, where the imaginary modes are given the lowest possible frequencies by rescaling the low-temperature Debye law region.

S4.3 Experiment-theory dispersion comparison

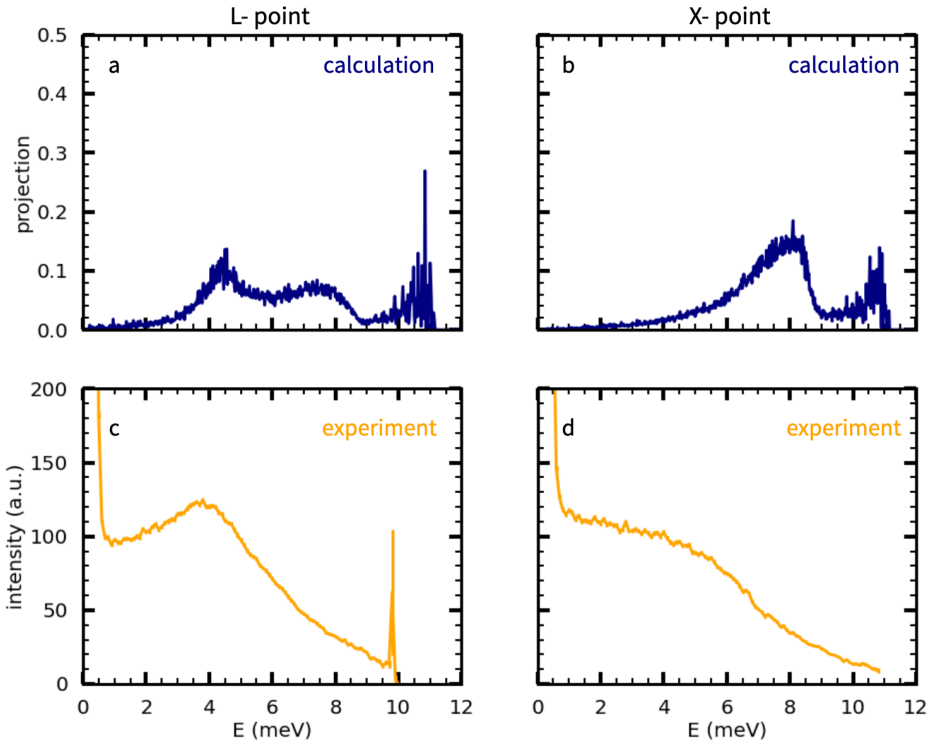

Figure S8: Comparison between cuts of the phonon spectra at chosen points in the Brillouin zone of the disordered phase. Point $L = [0.5, 0.5, 0.5]$ (integrated between $[2.25, 2.25, -3.75]$ and $[2.75, 2.75, -3.25]$ in experiment) and point $X = [0, 1.0, 0]$ (integrated between $[2.75, 2.75, -2.25]$ and $[3.25, 3.25, -1.75]$ in experiment). At the L-point, the feature at 4 meV is reproduced. Features at higher energies do not occur in the experiment, likely because of neutron weighting. Neutron weighting has not been accounted for in the calculation of the disordered phase since neutron weighting software is currently not compatible with the SCLD method. However, the neutron weighting in the ordered phase (figure S9) shows that high-energy modes are downweighted in the neutron structure factor. This will likely be replicated in the disordered phase, which explains the absence of high-energy features in the experimental neutron data.

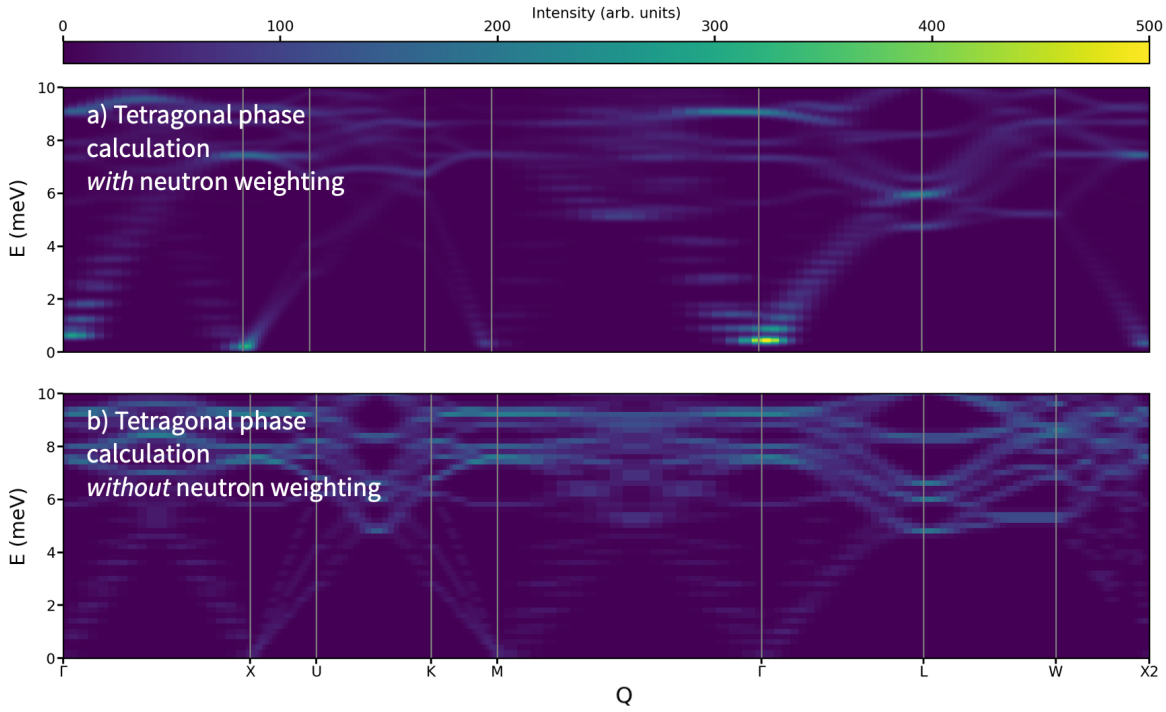

Figure S9: Calculated dispersion relation of adamantane's low-temperature phase, with (a) and without (b) neutron weighting. Most of the high-energy (> 5 meV) features are downweighted in the neutron structure factor.

S5 Brillouin zone labels

Point	Wavevector coordinates
Γ	$[0,0,0]$
X	$[0,1,0]$
L	$[0.5,0.5,0]$
W	$[0.5,1,0]$
U	$[0.25,1,0.25]$
W_2	$[0,1,0.5]$
K	$[0.75,0,0.75]$

Table S4: Labels of high-symmetry points in the Brillouin zone of space group $Fm\bar{3}m$. Wavevector coordinates are in conventional basis. In the neutron experiment, the path using these points was centred at $\Gamma = [3,3,-3]$.

Point	Wavevector coordinates
Γ	$[0,0,0]$
X	$[0,0.5,0]$
M	$[0.5,0.5,0]$
Z	$[0,0,0.5]$
R	$[0,0.5,0.5]$
A	$[0.5,0.5,0.5]$

Table S5: Labels of high-symmetry points in the Brillouin zone of space group $P\bar{4}2_1c$.

References

[1] M. Bee, J. P. Amoureux, R. E. Lechner, *Molecular Physics* **1980**, *40*, 617–641.

[2] M. M. Bée, *Quasielastic neutron scattering : principles and applications in solid state chemistry, biology, and materials science*, Adam Hilger, **1988**, p. 437.

[3] R. E. Lechner, A. Heidemann, *Commun. Phys.* **1976**, *1*, 213.

[4] D. F. Shanno, *Mathematics of Computation* **1970**, *24*, 647–656.

[5] A. P. Thompson, H. M. Aktulga, R. Berger, D. S. Bolintineanu, W. M. Brown, P. S. Crozier, P. J. in 't Veld, A. Kohlmeyer, S. G. Moore, T. D. Nguyen, R. Shan, M. J. Stevens, J. Tranchida, C. Trott, S. J. Plimpton, *Computer Physics Communications* **2022**, *271*, 108171.

[6] D. W. Greig, G. S. Pawley, *Molecular Physics* **1996**, *89*, 677–689.

[7] R. L. Fair, J. L. Farmer, A. J. Jackson, J. C. King, M. D. Le, T. G. Perring, C. Pettitt, K. Refson, G. S. Tucker, D. J. Voneshen, *Euphonic*, `https://euphonic.readthedocs.io`.

[8] A. R. Overy, A. Simonov, P. A. Chater, M. G. Tucker, A. L. Goodwin, *Physica Status Solidi (B) Basic Research* **2017**, *254*, 1600586.

[9] T. B. Boykin, N. Kharche, G. Klimeck, *European Journal of Physics* **2006**, *27*, 5–10.

[10] S. A. Wells, M. T. Dove, M. G. Tucker, *Journal of Physics Condensed Matter* **2002**, *14*, 4567–4584.

[11] S. A. Wells, A. Sartbaeva, *Molecular Simulation* **2015**, *41*, 1409–1421.